ELSEVIER

Coordination Chemistry Reviews
214 (2001) 187–213

COORDINATION CHEMISTRY REVIEWS

www.elsevier.com/locate/ccr

Photoelectron spectra of metal-containing molecules with resolutions better than 1 meV☆

Dong-Sheng Yang *

Department of Chemistry, University of Kentucky, Lexington, KY 40506-0055, USA

Received in revised form 24 July 2000

Contents

Abstract

This article describes the applications of zero electron kinetic energy, ZEKE, photoelectron technique to metal-containing molecules. Examples include vanadium dimer, metal

☆ 1 meV = 8.06554 cm^{-1} = 23.0605 cal mol^{-1}

* Tel.: +1-859-2574622; fax: +1-859-3231069.
E-mail address: dyang0@pop.uky.edu (D.-S. Yang).

PII: S0008-6215(00)00391-X

trimer compounds (Nb_3O, Nb_3C_2, Nb_3N_2, Zr_3O, and Y_3C_2), and metal atom-molecule complexes ($InNH_3$, $AlNH_3$, $ZrO(CH_3)_2$, and $YO(CH_3)_2$). The bond length of vanadium dimer cation has been determined from the rotationally resolved spectra with a resolution of 1.5 cm^{-1}, or 0.19 meV. The geometric conformations and electronic states of the clusters and complexes have been identified by combining the vibrationally resolved spectra and Franck–Condon factor calculations. The vibrational spectra have linewidths of 4–8 cm^{-1}.

Keywords: Photoelectron; ZEKE; Metal cluster; Metal complex

1. Introduction

1.1. General approaches of photoelectron spectroscopy

In molecular photoelectron spectroscopy (PES), a photon provides the energy to ionize a molecule with the ejection of an electron: $M + h\nu \rightarrow M^+ + e^-$. The energy difference (ΔE) between a final ion state and an initial neutral state equals the incident photon energy ($h\nu$) minus the kinetic energy (KE) of an emitted electron, that is, $\Delta E = h\nu - KE$. By defining ionization energy (IE) as the minimum energy required to remove an electron from the neutral ground state (i.e. the energy difference between the ground states of the neutral and ion), then $\Delta E = IE + E_{ion} - E_{neutral}$, where E_{ion} and $E_{neutral}$ are internal energies of the ion and neutral states, which can be electronic, vibrational, and rotational levels. If molecules are initially at their ground state, photoelectron spectroscopy determines the energies of various ion states. If molecules are populated at some excited levels, the energies of these neutral levels may also be determined in addition to those of ion states. There are two general ways to do photoelectron spectroscopy. One is to measure the kinetic energies of emitted electrons at a fixed photon wavelength. This approach does not require a tunable light source and is relatively simple to implement experimentally. Thus, the approach has been widely used since the inception of the photoelectron technique in the 1960s [1], and most of photoelectron spectra of metal compounds have been reported with this method [2–6]. However, although there is no fundamental limitation to the spectral resolution of PES, the practical resolution has been limited by the difficulties in separating electrons with small energy differences, and vibrational energy levels have rarely been resolved in the spectra of metal compounds [2–6]. For the convenience of the discussion, this method will be referred to as conventional PES.

A different approach is that photon wavelengths are tuned across various ionization thresholds, and electrons with a given kinetic energy are detected. When the energy of the incident photon is equal to the transition energy of an initial neutral state to a final ion state, electrons are emitted with zero electron kinetic energy (ZEKE). If only ZEKE electrons are detected, the technique is termed ZEKE PES or threshold PES. The principal advantage of the ZEKE technique is its very high spectral resolution.

1.2. ZEKE photoelectron detection

There have been several excellent reviews [7–9] and a recent book on ZEKE spectroscopy [10]. The reader is referred to these for further details. Briefly, the key idea of the ZEKE technique is the use of a time delay between photoionization and electron detection. Assuming that photoionization occurs in a field-free sphere (Fig. 1), after a suitable time delay the kinetic electrons (labeled 2–5) formed whenever $h\nu > \Delta E$ will have moved out of the ionization region, but the ZEKE electron (labeled 1) will have stayed at the point where it was produced because of its zero velocity. If an electric pulse (E_p) is applied, the electrons that have moved apart will be accelerated to a different velocity from the ZEKE electron and arrive at the detector at a different time-of-flight. The off-axis electrons (labeled 4 and 5) do not reach the detector because of their perpendicular velocity component. Therefore, if one sets a detection window at the right time, it is possible to record the ZEKE signal without the interference from the other electrons. Direct photoionization ZEKE method has been used to study a number of metal anions [11–14], but has proved rather difficult to implement experimentally.

In addition to direct photoionization, ZEKE electrons can also be generated by delayed pulsed-field-ionization (PFI) of long-lived (up to tens of μs), high-lying (with principal quantum number $n > 150$) Rydberg states, as shown in Fig. 2. In this way, electrons are first photoexcited to the high-lying Rydberg states, which are just few cm^{-1} below the ionization threshold. After a time delay from photoexcitation, an electric pulse is switched on to ionize the Rydberg states. Because cross sections are continuous through threshold, the Rydberg electrons produced by the

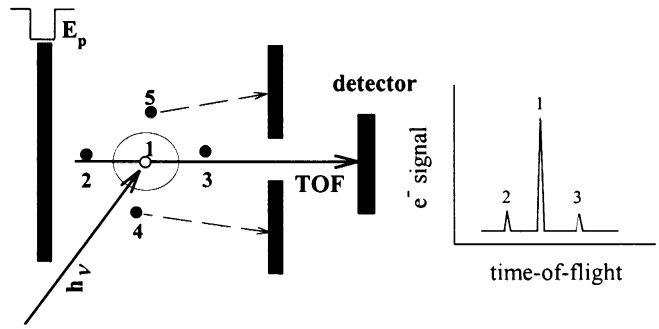

Fig. 1. ZEKE photoelectron detection scheme. ZEKE (point 1) and kinetic electrons (points 2–5) are produced with a tunable light source ($h\nu$). After a suitable time delay from photoionization, the kinetic electrons move out ionization sphere, whereas the ZEKE electron remains where it was formed. By applying an electric field E_p, the ZEKE electron and kinetic electrons (2 and 3) are accelerated to the detector at a different time-of-flight (TOF). The off-axis electrons (4 and 5) do not reach the detector because of steradiancy discrimination. The ZEKE electron can be detected by setting a detection window at the right time.

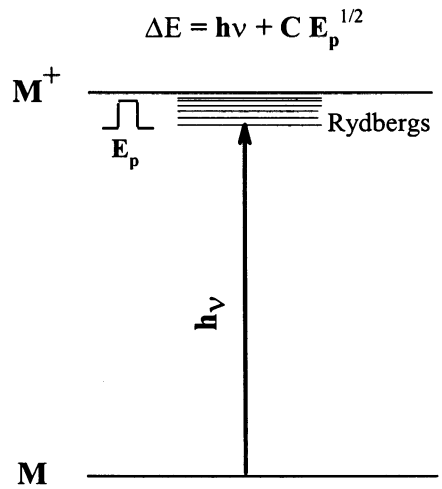

Fig. 2. The generation of ZEKE electrons by delayed pulsed-field-ionization (PFI). In this scheme, a molecule is first photoexcited to Rydberg states, which are just few cm^{-1} below the ionization threshold, and then ionized with a delayed electric field (E_p). The transition energy (ΔE) from the neutral state to the ion state is the summation of the incident photon energy ($h\nu$) and the energy shift induced by the ionizing field, which is proportional to the square root of the field strength.

field ionization carry, in principle, the same information as the free ZEKE electrons generated by threshold ionization. Thus, these Rydberg electrons are called PFI-ZEKE or ZEKE electrons. With a slight energy correction (δ) induced by the ionizing field, a ZEKE spectrum is produced as photon wavelengths are scanned. The energy shift can be calculated according to $\delta = CE_p^{1/2}$, where δ is in cm^{-1} and E_p is in V cm^{-1}. The constant, C, can be determined by measuring the ZEKE signals at various electric fields. The longevity of the high-lying Rydberg states is a complicated issue and is currently attributed to the angular moment l mixing due to the weak dc field present in the excitation volume and the magnetic momentum m_l mixing due to the inhomogeneous electric field formed by nearby prompt ions. The advantage of the delayed field ionization over direct photoionization is its high collection efficiency of the ZEKE electrons. This is because stray fields inside apparatus cause the free ZEKE electrons produced by direct photoionization to move during the time delay, but they have no effects on the ZEKE Rydberg states. Therefore, the PFI-ZEKE detection scheme has become the most useful variant of ZEKE spectroscopy. The PFI technique, however, is not applicable to photodetachment of negative ions because no Rydberg states exist in such species.

Furthermore, one distinguishes between one-photon and multi-photon ZEKE spectroscopy. In a single-photon experiment, optical excitation links the ground electronic state (or thermally populated low-lying excited states) of the neutral molecule to an electronic state of the corresponding cation. Single-photon ZEKE is particularly useful for molecules with no known electronic transition, such as most metal compounds. In a multi-photon experiment, an electronic transition of the

neutral species is normally used to select an intermediate state before accessing the high-lying Rydberg levels. Obviously, resonant multi-photon ZEKE can only be applied to the species for which electronic transitions are known.

The first advantage of ZEKE PES over the conventional PES is its high spectral resolution. Fig. 3 demonstrates the resolution difference of these two PES techniques by comparing the spectra of niobium trimer oxide [15,16]. The conventional PE spectrum (top) shows a broad band with a bandwidth of 35 meV. The ZEKE spectrum (bottom) displays a fully resolved vibrational structure with a line width of 0.6 meV. The ZEKE spectrum has a resolution of about 60 times better than the conventional PE spectrum. In principle, the resolution of a ZEKE spectrum can be improved by using a smaller ionizing pulse. In this case, however, the resolution was compromised with the detection sensitivity. As we will see in Section 3.1, a resolution of 0.19 meV has been achieved in the spectrum of a metal dimer [17]. Second, the IEs of many metal compounds are in a spectral region easily accessible by frequency-doubled tunable dye lasers, making applications of the technique fairly routine. Third, some vibrational normal modes of metal compounds are sufficiently small so that they may be thermally populated at room temperature, making it possible to measure the vibrational frequencies of the neutral, in addition to the corresponding ion.

In the following, I will describe the experimental setup and procedures to obtain ZEKE spectra in molecular beams and present examples to demonstrate the

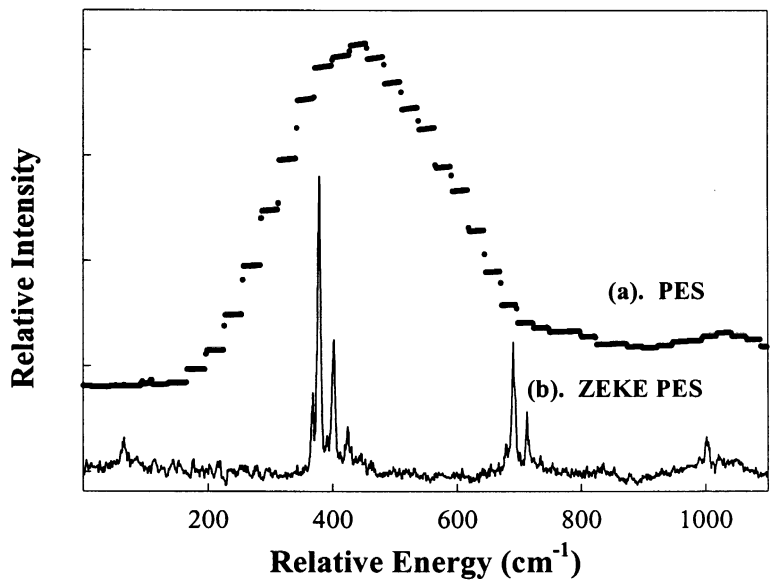

Fig. 3. Spectra of triniobium monoxide obtained by (a) recording kinetic electron signals produced at a fixed photon energy and (b) collecting ZEKE electrons while photon wavelengths were scanned. The conventional PE spectrum (a) has a resolution ca. 35 meV, and the ZEKE spectrum (b) has a resolution of 0.6 meV [15,16].

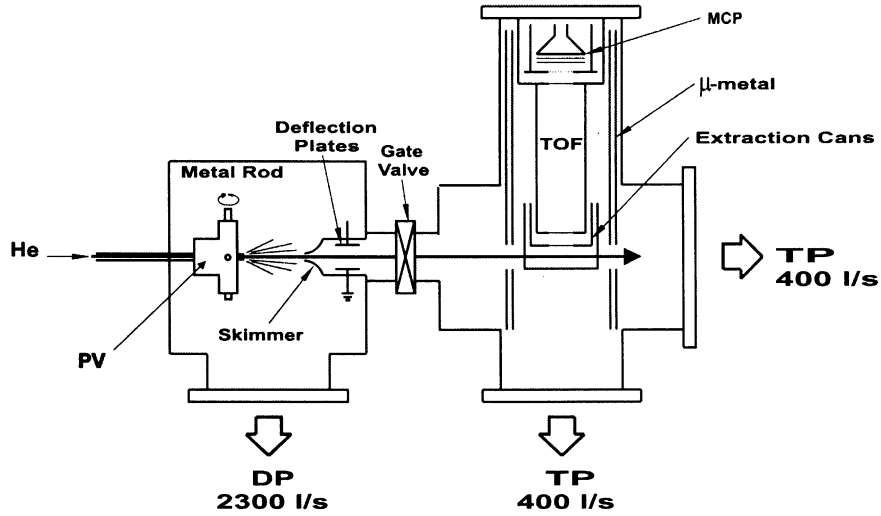

Fig. 4. Schematic of the molecular beam ZEKE photoelectron spectrometer system. PV, piezoelectric pulsed valve; DP, diffusion pump; TP, turbomolecular pump; TOF, time-of-flight tube; MCP, microchannel plate detector.

applications of the ZEKE technique to metal-containing molecules. The examples include the determination of the bond length of a cationic metal dimer from rotationally resolved spectra, the determination of geometric conformations of covalent metal trimer compounds from vibrationally resolved spectra, and the identification of electrostatic association complexes formed by the interactions between metal atoms and neutral molecules. The rotational spectra were obtained by two-photon excitation, and the vibrational spectra were recorded with single-photon excitation. The interpretation of the vibrational spectra and the determination of the molecular geometries were facilitated by density functional theory (DFT) calculations and spectral simulations based on the Franck–Condon (FC) principle.

2. Experimental

Fig. 4 shows the schematic of the metal molecular beam ZEKE spectrometer system. It consists of two vacuum chambers. The first chamber houses a Smalley-type cluster source [18] pumped by a 2200 l s^{-1} oil diffusion pump (Edwards). The second chamber houses the ZEKE spectrometer pumped by two 400 l s^{-1} turbomolecular pumps (Seiko Seiki). A gate valve separates the two chambers.

The cluster source consists of a piezoelectric pulsed valve to deliver intense gas pulses [19]; a motor driven mechanism to rotate and translate a metal rod to ensure each laser pulse vaporizes a fresh surface of the metal target; a clustering tube to help maximize the production of the species of interest; a skimmer to collimate the

molecular beam; and a pair of deflection plates to remove the residual ionic species, which are formed in the laser ablation process, from entering the second chamber. The clustering tube can be operated in the temperature range of 77–700 K.

The ZEKE spectrometer is a two-field, space-focused, Wiley–McLaren time-of-flight mass spectrometer [20]. It consists of a two-stage extraction assembly, a 34 cm long flight tube, and a dual microchannel plate detector (Galileo). The extraction elements, which have cylindrical symmetry, are extended up along the sides of the flight tube to prevent field penetration from the dc voltages applied to the detector. To prevent the electron trajectories being influenced by the stray fields, including the earth's magnetic field, the entire spectrometer is encased in a double-wall cylindrical μ-metal shield, which is pierced only by apertures required to admit the molecular and laser beams.

Metal-containing molecules were produced with a Nd:YAG laser vaporization (532 or 355 nm, Lumonics YM 200/800) of a metal rod (> 99.9%) in the presence of a pulse of helium gas doped with small amount of a reactant (of course, no reactant was added for making bare metal clusters). Prior to single-photon ZEKE measurements, three steps were carried out to help identify the carrier of the ZEKE electrons. First, the molecules formed in supersonic jet were identified with single-photon photoionization time-of-flight mass detection. The ionization light was provided by a frequency-doubled dye laser (Lumonics HD500). A 320 V cm^{-1} dc field was used to extract positive ions. This field strength gave the best possible mass resolution of the spectrometer. Second, the production and selection of the molecule of interest were maximized by optimizing the time and power of the vaporization and excitation lasers, reactant concentrations, and backing pressures of sample gases. Third, the ionization threshold of the molecule was measured by recording the molecular ion signal as the frequency-doubled dye laser was scanned in an appropriate wavelength region.

ZEKE spectral measurements were performed by first photoexcitation of the molecule to high-lying Rydberg levels and then delayed field ionization of the Rydberg states. To extract ZEKE electrons from the Rydberg states, a negative electric pulse provided by a commercial pulse delay generator (Stanford DG535) was applied to the lower extraction can, but the upper can was grounded. Energy shifts (δ) induced by electric pulses (E_p) could be determined by recording ZEKE signal at various pulsed field strengths and were determined to follow the relationship $\delta = 4.1\ E_p^{1/2}$ in the case of vanadium dimer [17]. For larger molecules, low signal levels precluded a systematic study of the field dependence of the ZEKE spectra. However, in a field range of 0.8–1.2 V cm^{-1}, no significant changes were observed in the ZEKE peak positions. Furthermore, the effects of varying laser-extraction pulse delay, pulse amplitude, pulse width, and dc offset were investigated to find the optimum conditions for recording ZEKE spectra. A pulse of 1.2 V cm^{-1}, 100 ns duration, delayed by ca. 3 μs after laser excitation was found to give the best compromise between sensitivity and resolution. A small dc offset, typically 0.08 V cm^{-1}, was used to reject electrons from direct laser ionization. The residual field in the ZEKE spectrometer was determined to be less than 0.01 V cm^{-1} by measurements on atoms with precisely known IEs. ZEKE electron signals were

capacitively decoupled from the dual microchannel plate anode, amplified by a preamplifier (Stanford SR445 300 MHz), and averaged by a gated integrator (Stanford SR250). The averaged output was fed to a computer, which also controlled the scanning of the dye lasers. Experimental repetition rate was 10 Hz, and 30 samples were typically accumulated at each data point. ZEKE spectra were recorded as a function of the laser wavelengths, which were calibrated against appropriate atomic transitions.

3. Applications of ZEKE technique to metal-containing molecules

3.1. Rotational spectra and bond length of vanadium dimer

The neutral V_2 molecule was first studied with resonant two-photon ionization spectroscopy, and a rotationally resolved $A^3\Pi_u \leftarrow X^3\Sigma_g^-$ band system was reported with the origin near 700 nm [21]. The IE of the molecule was also measured to be around 51270 cm^{-1} with resonant two-photon threshold photoionization [22]. The cation V_2^+ was predicted to have a ground state of $^4\Sigma_g^-$ [23]. With the known intermediate state ($A^3\Pi_u$) and IE of the molecule, V_2 was thought to be an ideal case for testing the ZEKE technique. Fig. 5 displays typical ZEKE spectra of V_2, obtained by two-photon excitation through the transitions in the $A^3\Pi_u \leftarrow X^3\Sigma_g^-$ system [17]. The $^3\Pi_u$ state has three spin-orbit components: $^3\Pi_{2u}$ ($\Omega = 2$), $^3\Pi_{1u}$

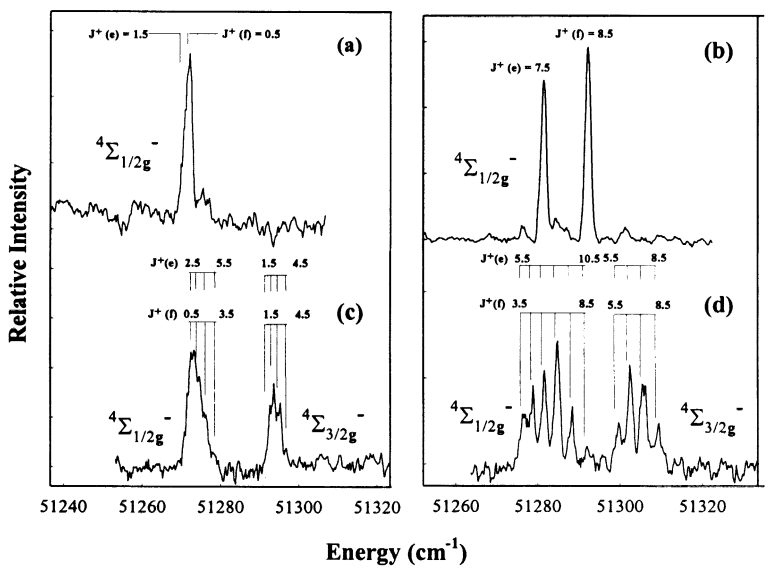

Fig. 5. ZEKE spectra of V_2 recorded with the excitation laser tuned to the rotational lines Q(1) (a) and R(7) (b) in the $A^3\Pi_{1u} \leftarrow X^3\Sigma_{0g}$ (0,0) band and to the rotational lines Q(2) (c) and R(6) (d) in the $A^3\Pi_{2u} \leftarrow X^3\Sigma_{1g}$ (0,0) band [17].

($\Omega = 1$), and $^3\Pi_{0u}$ ($\Omega = 0$) (Ω is total electronic angular momentum about internuclear axis and can be obtained by an algebraic addition of total orbital (Λ) and spin (Σ) angular momenta, $|\Lambda + \Sigma|$, along the molecular axis [24]). Similarly, the $^3\Sigma_g^-$ground state has spin components of $^3\Sigma_{1g}^-$ ($\Omega = 1$) and $^3\Sigma_{0g}^-$ ($\Omega = 0$). The spectra in Fig. 5(a,b) were obtained by exciting the rotational lines Q(1) and R(7) of the $A^3\Pi_{1u} \leftarrow X^3\Sigma_{0g}^-$ (0,0) band, and those in Fig. 5(c,d) were recorded with the excitation of the Q(2) and R(7) lines of the $A^3\Pi_{2u} \leftarrow X^3\Sigma_{1g}^-$ (0,0) band. The ZEKE spectral linewidth is 1.5 cm^{-1} (0.19 meV), which is sufficient to resolve the rotational energy levels of the ground state of V_2^+. There are striking differences between the spectra recorded through the $^3\Pi_{1u}$ and $^3\Pi_{2u}$ components. First, The spectra through the $^3\Pi_{1u}$ component show only the transitions to the $^4\Sigma_{1/2g}^-$ level (Fig. 5(a,b)), whereas the spectra through the $^3\Pi_{2u}$ component show the transitions to both the $^4\Sigma_{1/2g}^-$ and $^4\Sigma_{3/2g}^-$ levels (Fig. 5(c,d)). This observation is consistent with the $\Delta\Sigma = \pm 1/2$ spin selection rule of photoionization of a diatomic molecule derived by Xie and Zare [25]. Σ is 3/2 for the $^4\Sigma_{3/2g}^-$ state ($\Sigma = \Omega = 3/2$), 1/2 for $^4\Sigma_{1/2g}^-$ ($\Sigma = \Omega = 1/2$), 1 for $^3\Pi_{2u}$ ($\Sigma = \Omega - \Lambda = 2 - 1 = 1$), and 0 for $^3\Pi_{1u}$ ($\Sigma = \Omega - \Lambda = 1 - 1 = 0$). The ZEKE spectra also confirm the $^4\Sigma_g^-$ symmetry of the cation ground state predicted by the DFT calculations [23]. The second major difference is that when probing from the $^3\Pi_{1u}$ component, only two J^+ values were accessed, while probing from the $^3\Pi_{2u}$ level, a wide range of J^+ values were observed. Detailed analysis of the rotational spectra was based on the Xie and Zare selection rules [25] and the rotational Hamiltonian matrix for a $^4\Sigma^-$ state in a Hund case (a) [26]. The spectral analysis has lead to the first determination of the bond length, $r_0 = 1.7347$ (24) Å, of the $X^4\Sigma_g^-$ state of V_2^+. It is 0.034 Å shorter than that of the $X^3\Sigma_g^-$ state of V_2 [21]. The difference in the bond lengths provides a further evidence for the fact that $V_2^+(D_0^0 = 3.140$ eV) is more strongly bound than V_2 ($D_0^0 = 2.753$ eV) [22,23]. In addition to the bond length, other spectroscopic parameters of the $X^4\Sigma_g^-$ state determined from the ZEKE spectra include adiabatic IE, 51271.14(50) cm^{-1}; second-order spin-orbit splitting (i.e. the energy difference between the $^4\Sigma_{1/2g}^-$ and $^4\Sigma_{3/2g}^-$ spin states), 20.992(68) cm^{-1}; rotational constant, 0.21993(59) cm^{-1}; and spin-rotation constant, 0.0097(87) cm^{-1}.

3.2. Vibrational spectra and geometric conformations of metal trimer compounds

The ZEKE spectra of metal cluster compounds were recorded with single-photon excitation because there is no known electronic transition reported for these molecules and the their IEs are expected to be in the wavelength region accessible with frequency-doubled dye lasers. The ZEKE spectra provide the first spectroscopic evidence of oxygen, carbon, and nitrogen binding to niobium, zirconium, and yttrium trimers.

3.2.1. Nb_3O and Zr_3O

Fig. 6 presents the spectra of Nb_3O recorded at 300 and 100 K [15]. The 300 K spectrum shows a short progression (bands labeled 0, 1, and 2), with an energy interval of 312 cm^{-1}. Superimposed on the progression are the hot bands (bands

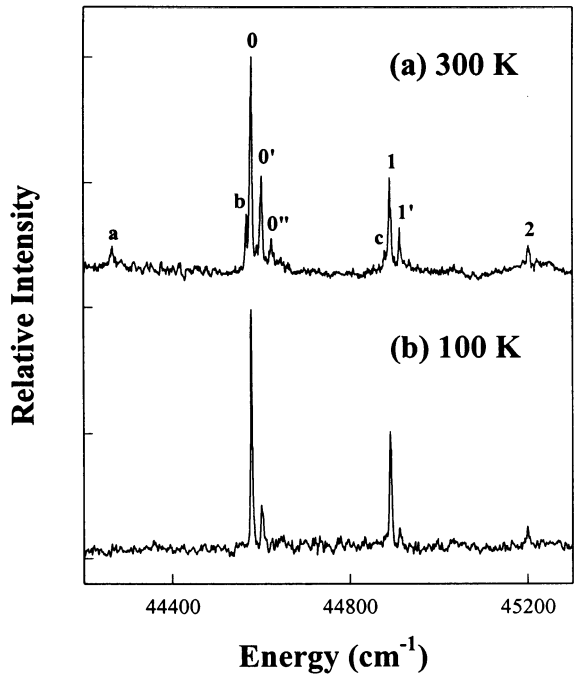

Fig. 6. ZEKE spectra of Nb_3O recorded at 300 K (a) and 100 K (b) [15].

labeled a, b, c, 0′, 0″, and 1′) from an excited vibrational level of the neutral Nb_3O because their intensities decrease at 100 K. Band a is 320 cm^{-1} to the red of band 0. The linewidth of the 300 K spectrum is 5 $cm^{-1}$and is reduced to 4 cm^{-1} at 100 K. The linewidth reduction is attributed to a narrowing of rotational envelope at the lower temperature. Some preliminary conclusions can be drawn from the spectra. First, the 312 cm^{-1} interval most likely arises from one of the niobium symmetric vibrations in the ion because a symmetric niobium–oxygen vibration would have a much higher frequency [27]. The 320 cm^{-1} spacing may be related to the corresponding niobium mode in the neutral cluster. Second, the geometries of the neutral and the cation are rather similar because only a short progression appears in the spectra.

To assign the spectra in detail and to extract geometric information from the spectra, spectral simulations were carried out by calculating multidimensional FC factors using the DFT geometries, harmonic vibrational frequencies, and normal mode coordinates of Nb_3O and Nb_3O^+. Fig. 7 presents the minimum energy structures and relative energies of Nb_3O and Nb_3O^+, as calculated with the deMon-KS-LSDA DFT method [28]. These geometries were obtained by minimizing the total energy without symmetry constraint. The most stable structure of both Nb_3O and Nb_3O^+ is planar with C_{2v} symmetry. The oxygen atom is bound with equal bond lengths to two Nb atoms. Two distinct Nb–Nb bond distances are

present in the cluster with the Nb–Nb bond bridged by oxygen being longer than the other two. The ground electronic symmetry of the C_{2v} structure is $^2B_1$ for the neutral and $^1A_1$ for the ion. A second stable structure is three-dimensional with oxygen bound to three Nb atoms. This structure lies 1.03 eV (23.7 kcal mol^{-1}) higher than the planar one for both the neutral and ion. The geometric symmetry of the three-dimensional structure is C_s for the neutral and C_{3v} for the ion. The lower symmetry of the neutral molecule may be due to Jahn–Teller distortion.

FC factors were calculated by assuming that the neutral and ion potentials are both harmonic. The method described below was applied to all molecules discussed in this article. Normal coordinates for the neutral and ion are linear combinations of Cartesian displacements of the atoms from the neutral or ion equilibrium geometry. The normal coordinates of the neutral and ion differ because the equilibrium geometries are different and the linear combinations of the atomic displacements are different. Normal coordinates for the neutral and ion are denoted by q and q', respectively, and are defined in terms of the Cartesian displacements of the atoms by

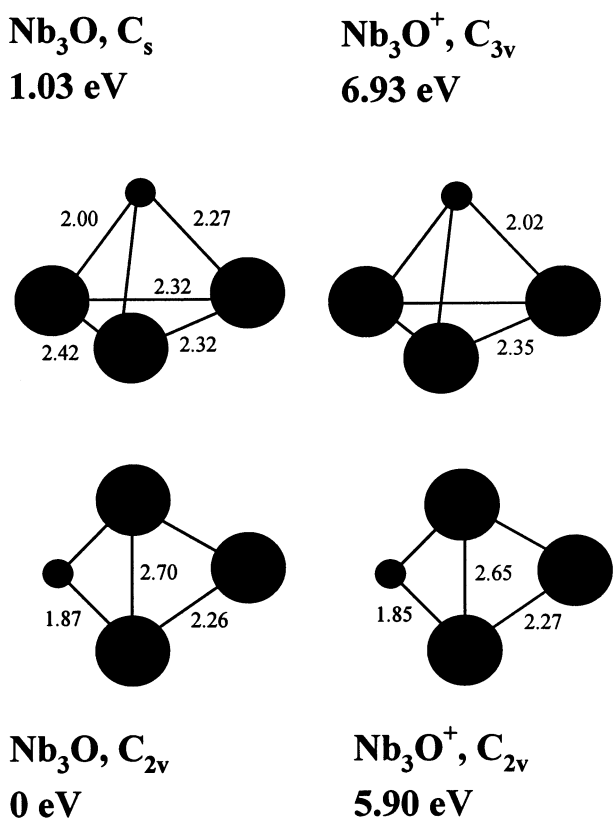

Fig. 7. Calculated geometries and relative energies of Nb_3O and Nb_3O^+. Bond lengths are in Å [15].

$$q' = (L')^{T}d \tag{1}$$

and

$$q = (L)^{T}d \tag{2}$$

The L and L′ matrices are determined by diagonalizing mass-weighted Cartesian force constant matrices for the neutral and ion. The two sets of normal coordinates are related [29],

$$q' = Sq + Q \tag{3}$$

where

$$S = (L')^{T}L \tag{4}$$

and

$$Q = (L')^{T}D \tag{5}$$

D being the vector of the differences of the mass-weighted Cartesian coordinates at equilibrium for the neutral and ion. The fact that S is not an identity matrix, because the normal coordinates of the ion are rotated with respect to those of the neutral, was first pointed out by Duschinsky [30].

Assuming that the potentials of the neutral and ion are adequately described by an harmonic approximation makes it possible to calculate the FC overlaps in closed form (without setting $S = 1$ or neglecting differences between the neutral and ion frequencies) using recursion relations given by Doktorov et al [31]. Using the L matrices computed by the DFT calculations, the S matrix was found to be very close to the identity and the components of Q vector were substantial. In such a case, a good approximation to the FC structure of a cold spectrum was obtained by using a displacement parameter expressed in terms of the final ion state [32,33]. In this case, the intensity of a transition between two vibrational states is due to the displacement of the two electronic surfaces. The displacement of the *i*th normal coordinate, B_i, determines the intensity of the *i*th totally symmetric mode,

$$B_i = (\omega_i/h)^{1/2}Q_i \tag{6}$$

Here Q_i is a component of the vector Q defined above. This treatment reduces the FC integral to the product of one-dimensional integrals.

Spectral broadening was simulated by giving each line a Lorentzian lineshape with the FWHM (full width at half maximum) of the experimental spectra.

Fig. 8 displays the experimental spectrum (a) and the simulations from both the planar (b) and three-dimensional (c) geometries [15]. The theoretical transition energies are plotted relative to the position of the 0 band of the experimental spectrum. A remarkable agreement exists between the experiment and theory for the planar structure. However, the simulation from the three-dimensional structure is very different from the experimental spectrum. Thus, the comparison indicates that Nb_3O and Nb_3O^+ probed in the ZEKE experiment have the planar C_{2v} structure, rather than the three-dimensional one. The good agreement between the

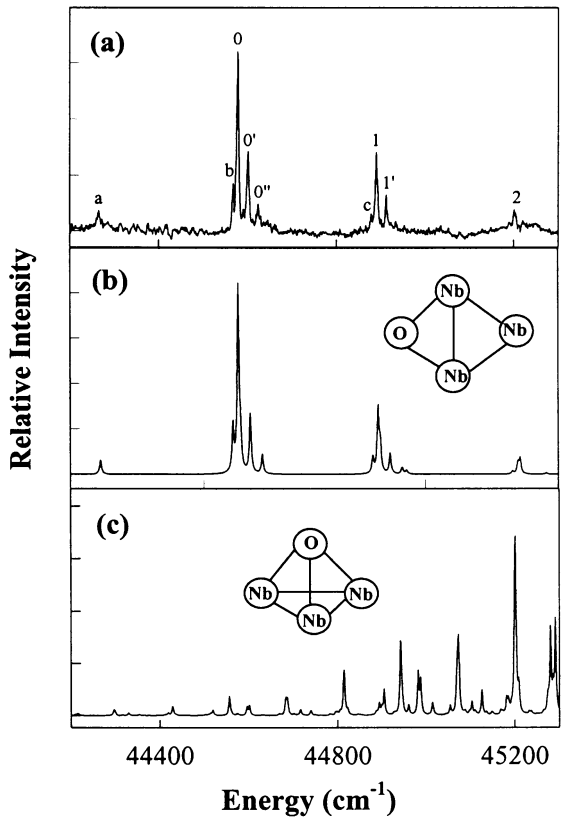

Fig. 8. Experimental (a) and simulated (b,c) ZEKE spectra of Nb_3O at 300 K. The simulations were performed with the geometries and vibrational frequencies obtained from the deMon-KS-LSDA DFT calculations [15].

experiment and the simulation of the planar structure makes the spectral assignment trivial. The origin band is the band 0, which measures the IE of the cluster to be 44578 cm^{-1}. The 312 cm^{-1} main progression (bands 0, 1, and 2) arises from the transitions of the vibrational ground state of Nb_3O to the vibrational levels of the niobium symmetric bend of Nb_3O^+. The hot band, band a, is due to the transition from the first vibrational level of the niobium symmetric bend mode of Nb_3O to the vibrational ground state of Nb_3O^+. The frequency of the neutral bend mode is measured to be 320 cm^{-1}. Associated with the main progression, on the high frequency side of the main bands are the sequence bands (i.e. hot bands with the same vibrational quanta in the neutral and ion states) arising from the niobium asymmetric stretch motions. The energy difference of the asymmetric mode in Nb_3O^+ and Nb_3O is determined to be 23 cm^{-1} On the low energy side of the main progression are the sequence bands due to the out-of-plane deformation of the cluster. The deformation mode is 11 cm^{-1} smaller in the ion than in the neutral.

The general features of the ZEKE spectrum of Zr_3O (not shown) are similar to those of Nb_3O [16]. The zirconium symmetric bend of Zr_3O^+ is measured as 272 cm^{-1}, 40 cm^{-1} lower than the corresponding niobium mode in Nb_3O^+. The IE of Zr_3O is 41838 cm^{-1}, 2740 cm^{-1} lower than the IE of Nb_3O. The structure of Zr_3O and Zr_3O^+ is also planar with C_{2v} symmetry, as determined by the comparison of the experimental and simulated spectra.

3.2.2. Nb_3C_2 and Y_3C_2

The ZEKE spectra of the metal trimer carbides display higher vibronic activities than those of the oxides discussed above. Fig. 9(a) presents the spectrum of $Nb_3^{12}C_2$ at room temperature [34]. The spectrum consists of a strong vibrational progression (a_n) and six weak ones (b_n, c_n, d_n, e_n, f_n, and g_n). All seven progressions have the same energy interval of 258 cm^{-1}. Six of the seven progressions can be grouped into three pairs, a_n and b_n, c_n and d_n, and f_n and g_n, with the same energy separation of 20 cm^{-1}. The separation of d_n and e_n is 13 cm^{-1}. The f_n progression is 339 cm^{-1} from the main progression a_n. The a_n progression has a linewidth of 7 cm^{-1}, which decreases to 5 cm^{-1} at 100 K, due to the narrowing of rotational envelope. The

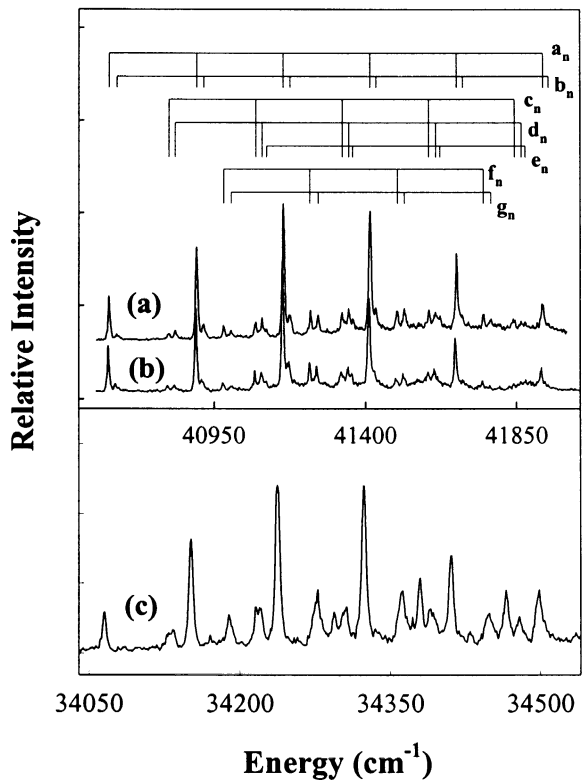

Fig. 9. ZEKE spectra of $Nb_3^{12}C_2$ (a); $Nb_3^{13}C_{12}$ (b); and $Y_3^{12}C_2$ (c) [34,36].

intensities of most small bands depend on the cluster source conditions. Fig. 9(b) shows the spectrum of $Nb_3^{13}C_2$, which has the same energy spacing and intensity profile as that of $Nb_3^{12}C_2$, but shifts to the red by ca. 3 cm^{-1}. It can be concluded from the two spectra that the geometries of the neutral and ion are rather different, as indicated by the relatively long progressions. One of the normal modes of the cluster ion has a vibrational frequency of 258 cm^{-1}. This mode is associated with the niobium motion because the energy interval of the progressions is independent of the carbon isotopes.

Triniobium dicarbide has two stable geometries: trigonal bipyramid and doubly bridged structures. The energy differences of the two neutral structures are predicted to be 0.02 eV by the Gaussian 94-B3P86 DFT calculations [35], implying that the two geometries are indistinguishable in terms of their energies. The trigonal bipyramid geometry has D_{3h} symmetry and $^1A_1'$ ground electronic state in $Nb_3C_2^+$. Adding an electron to the ion populates a degenerate orbital (e″), leading to a Jahn–Teller distorted neutral geometry with a lower symmetry. The electronic ground state of Nb_3C_2 is $^2A_1$ in C_{2v} symmetry. For the doubly bridged structure, both Nb_3C_2 and $Nb_3C_2^+$ have C_{2v} symmetry. The ground state of the doubly bridged structure is $^1A_1$ for the ion and $^2A_1$ for the neutral. Like niobium trimer monoxide, niobium trimer dicarbide also prefers a low electron spin state.

Fig. 10 shows the experimental spectrum and simulations from the trigonal bipyramid and doubly bridged structures of Nb_3C_2 [34]. A comparison of the experiment and theory indicates that the cluster has the trigonal bipyramid structure, instead of the doubly bridged one. The overall good agreement between the simulation of the trigonal bipyramid structure makes detailed spectral assignments possible. These assignments are summarized below. The main progression a_n is due to the transitions from the ground state of the neutral to the vibrational levels of the degenerate e′ mode in the ion. The e′ mode is identified as the symmetric bend of the niobium atoms with a frequency of 258 cm^{-1}. Because of the low symmetry of the neutral cluster, the degenerate e′ mode splits into two non-degenerate modes, a_1 and b_2. In the rigid molecular limit, this symmetry transformation would have a one-to-one correspondence. That is, only transitions from the neutral ground state to the vibrational levels involving an arbitrary number of quanta of one component of the e′ and an even number of quanta of the other component of the e′ mode are allowed. However, The DFT calculations indicate a rotation of the normal coordinates of the e′ mode of the ion with respect to the corresponding modes of the neutral. This rotation results in the e′ mode being a 30–50% mixture of the neutral a_1 and b_2 modes. The b_n, c_n, and d_n progressions are associated with the transitions, respectively, from the first excited level of the a_1, b_2, or their combination of the neutral to the vibrational levels of the e′ mode of the ion. The vibrational frequencies are measured to be 238 cm^{-1} for the a_1 mode and 83 cm^{-1} for the b_2 mode. The remaining progressions, e_n, f_n, and g_n, are associated with the niobium symmetric stretch motions. The stretch frequency is 326 cm^{-1} in the neutral and 339 cm^{-1} in the ion.

The ZEKE spectrum of Y_3C_2 (Fig. 9(c)) has a similar structure to that of Nb_3C_2 although the IE and vibrational frequencies of Y_3C_2 are much lower [36]. The IE of

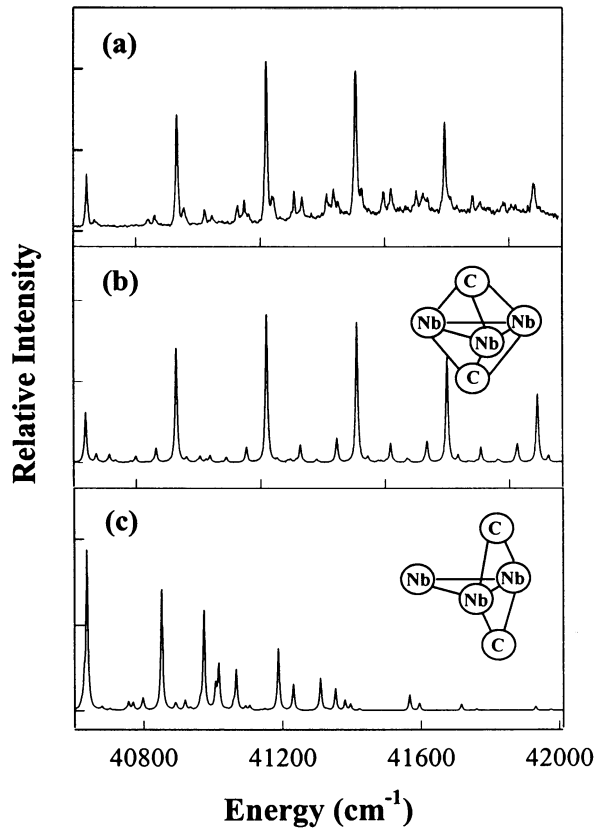

Fig. 10. Experimental (a) and simulated (b,c) ZEKE spectra of $Nb_3^{12}C_2$. The simulations were performed with the trigonal bipyramid and doubly bridged geometries and vibrational frequencies obtained from the Gaussian 94-B3P86 DFT calculations [34].

Y_3C_2 is measured to be 34065 cm^{-1}. The yttrium symmetric stretch mode has a frequency of 228 cm^{-1} in the ion. Two yttrium bend modes have frequencies of 82 and 24 cm^{-1} in the neutral and a degenerate frequency of 86 cm^{-1} in the ion. Unlike Nb_3C_2, the excitation of the yttrium stretch mode in the neutral was not observed in the spectrum of Y_3C_2 although the yttrium mode should have been thermally populated at room temperature.

The Gaussian 94-B3P86 DFT geometry optimizations found only a stable trigonal bipyramid structure for triyttrium dicarbide. The trigonal bipyramid geometry has either a C_{2v} or D_{3h} symmetry, depending on electron spin multiplicity. For the neutral cluster, the most stable states are doublet and quartet. The doublet has a $^2B_1(C_{2v})$ ground state, whereas the quartet has a $^4E'$ (D_{3h}) ground state. The $^2B_1$ state is 0.3 eV lower than the $^4E'$ state. The removal of an electron from the neutral states forms ionic states with possible multiplicities of 1, 3, and 5. These ionic states are calculated to be $^1A_1'$, $^3B_1$, and $^5A_2$, with the singlet state being the

lowest in energy and the highest in geometric symmetry (D_{3h}). From the electronic states of the neutral and ion, there are four electronically allowed ionization processes: $^1A_1' \leftarrow {}^2B_1$, $^3B_1 \leftarrow {}^2B_1$, $^3B_1 \leftarrow {}^4E'$, and $^5A_2 \leftarrow {}^4E'$. However, comparisons between the experimental and calculated spectra indicate that the most likely process is $^1A_1' \leftarrow {}^2B_1$.

3.2.3. Nb_3N_2

Fig. 11(a) shows the spectrum of Nb_3N_2 [37]. The spectrum is characterized by a short progression with the energy interval of 257 cm^{-1} and small bands on the high energy side of the progression. The spectral intensity profile appears much different from that of Nb_3C_2, but rather similar to that of Nb_3O. The 257 cm^{-1} spacing of the progression is very close to that of the main progression in the spectrum of Nb_3C_2. These observations indicate that the structure of triniobium dinitride does not change significantly upon ionization and one of the niobium vibrations has a frequency close to that of triniobium dicarbide.

Unlike triniobium dicarbide that has stable trigonal bipyramid and doubly bridged geometries, triniobium dinitride adopts only a doubly bridged C_{2v} geometry, with a neutral $^2B_1$ ground state and an ion $^1A_1$ ground state. The simulation of the $^1A_1 \leftarrow {}^2B_1$ transition is shown in Fig. 11(b). The comparison of the experiment and theory indicates that the 257 cm^{-1} progression is due to the niobium symmetric bend vibration in $Nb_3N_2^+$. The small bands on the blue side of the

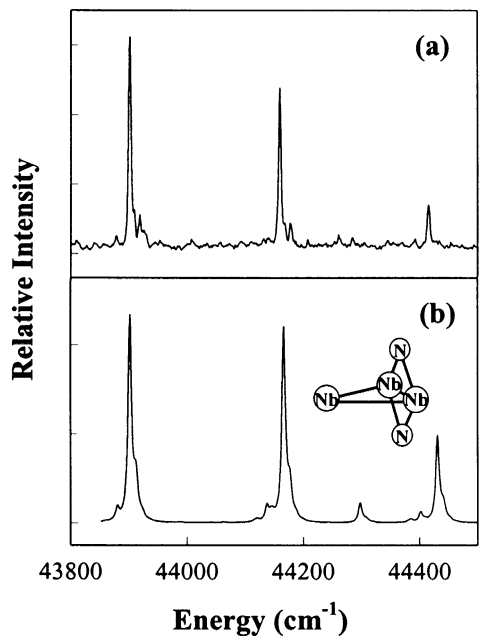

Fig. 11. Experimental (a) and simulated (b) ZEKE spectra of Nb_3N_2. The simulation was calculated using the doubly bridged geometry and vibrational frequencies from the ADF-BP DFT calculations [37].

Table 1
IEs (cm^{-1}) and vibrational frequencies (cm^{-1}) of metal clusters [a]

Cluster	IE	δ^+ (M_n) [b]	ν_s^+(M–M) [b]	δ (M_n) [b]	ν_s (M–M) [b]	Reference
Cluster	00 000[c]	000(000)	000(000)	000(000)	000(000)	Reference
Nb_3	46 858 [c]			227 [d]	335 [d]	[38,43]
Nb_3O	44 578	312(326)	(386)	320(322)	(366)	[15]
Nb_3C_2	40 639	258(278)	339(385)	237(250)	327(378)	[34]
Nb_3N_2	43 902	257(277)	(395)	(261)	(391)	[37]
Y_3	40 325 [c]					[39]
Y_3C_2	34 065	86(87)	228(245)	82 (92)	(232)	[36]
Zr_3	42 105 [c]			177 [d]	258 [d]	[40,44]
Zr_3O	41 838	(239)	272(288)	(236)	(281)	[16]

[a] Except where noted, values are from the ZEKE measurements. The uncertainty of the measurements is typically ca. 3 cm^{-1}, except for V_2 for which the uncertainty is ca. 0.5 cm^{-1}. The values in parentheses are from the density functional calculations and are averaged if results are available from more than one computational codes.

[b] δ^+ (M_n) and ν_s^+ (M–M) are metal symmetric bend and stretch in cluster ions. δ (M_n) and ν_s (M–M) are metal symmetric bend and stretch in neutral clusters.

[c] Photoionization efficiency measurements with the uncertainty of ± 400 cm^{-1}.

[d] Resonant Raman spectroscopic measurements in argon matrices.

progression are the sequence bands associated with a niobium asymmetric bend mode, which is 17 cm^{-1} smaller in the neutral than in the ion.

Table 1 summarizes IEs and vibrational frequencies of the metal cluster compounds. The IEs of the ligated metal trimers are lower than those of the corresponding bare metal clusters. The IE reduction upon carbon coordination is very similar for the niobium and yttrium trimers, but the reduction upon oxygen coordination is quite different between the niobium and zirconium clusters. For example, both Nb_3C_2 and Y_3C_2 have IEs ca. 6200 cm^{-1} (0.8 eV) lower than Nb_3 and Y_3 [38,39]. In contrast, the IE of Nb_3O is ca. 2300 cm^{-1} lower than that of Nb_3, whereas the IE of Zr_3O is only ca. 300 cm^{-1} less than that of Zr_3 [40].

The lower IEs of the cluster compounds than those of the corresponding bare clusters imply that the metal–ligand bonds are stronger in the ion than in the neutral compounds, on the basis of the thermodynamic cycle, D_0 (M_3^+–L)–D_0 (M_3–L) = IE (M_3)–IE (M_3L), where L = 2C, 2N or O. The stronger metal–ligand bonding is also evident from the higher metal–ligand stretch frequencies in the ion compounds. To help understand the ionization effect on the metal–ligand bonding in these clusters, we performed Mulliken population analysis for some of the clusters and found that in addition to covalent character, the metal–ligand bonding has considerable ionic character because of the combination of the electropositive metals and electronegative ligands. For example, orbital overlaps between Y and C are the same in Y_3C_2 and $Y_3C_2^+$, indicating that the covalent contribution to the Y–C bonds is similar in the neutral and ion. In contrast, the positive charge on Y increases from 0.46 in Y_3C_2 to 0.77 in $Y_3C_2^+$, whereas the negative charge on C

remains at −0.66 in both the neutral and ion. Thus, the stronger M_3^+–L bonds are largely due to the enhancement of the charge attraction in the ions.

Examination of the metal vibrational frequencies in Table 1 shows that the niobium vibrations have the highest frequencies and the yttrium vibrations have the lowest. Because the atomic masses of Nb, Zr, and Y are very similar, the higher frequencies mean stronger metal–metal bonds. Thus, the strengths of the metal–metal bonds may be arranged in the order of Nb–Nb > Zr–Zr > Y–Y in these compounds. Bonding differences among these metals have also been found for the bare metal dimers and trimers. For example, the bond dissociation energies of Nb_2, Zr_2, and Y_2 have been measured as 5.48, 3.05, and 1.62 eV, respectively [22,41,42]. The stretch frequency of Nb_3 is 335 cm^{-1}, whereas that of Zr_3 is 258 cm^{-1}, as measured from resonant Raman spectra in the argon matrices [43,44]. The main reason for the weak Y–Y bonding is the strong s-electron repulsion between the Y $4d^15s^2$ ground states. To form chemical bonds, at least one of the $4d^15s^2$ yttrium atoms must be promoted to a configuration such as $4d^25s^1$ to reduce the Pauli repulsion between the filled s-orbitals. The energy required to promote the yttrium s-electron from the $4d^15s^2$ to $4d^25s^1$ configuration is 1.36 eV. The promotion energy for the s-electron is 0.59 eV for the zirconium atom, and no promotion is necessary for the niobium atom because its ground state configuration is $4d^45s^1$. Thus, the bonding differences in these metal clusters are largely due to the different promotion energies required to prepare the metal atoms into appropriate electron configurations.

The M–M bonds are slightly stronger in the ions than in the corresponding neutrals, as indicated by the frequencies of the M–M stretch vibrations (Table 1). For example, the Nb–Nb stretch frequency is 327 cm^{-1} in Nb_3C_2 and 339 cm^{-1} in $Nb_3C_2^+$. For the other clusters, although experimental frequencies are not available for the comparisons, the theoretical values show a similar increase of the M–M stretch frequencies upon ionization.

3.3. Vibrational spectra and identifications of metal atom-molecule association complexes

Metal atom-molecule adducts are formed in the early portion of the reaction coordinates between metal atoms and neutral molecules. These precursors are considered to play an important role in determining subsequent chemical reactions and product distributions. However, the identification and characterization of this kind of complexes have been hindered because of their weak bonding. The following examples show that the ZEKE technique can be used to distinguish weakly-bound adducts from more strongly-bound insertion isomers formed in the reactions of laser-ablated metal atoms and small neutral molecules.

3.3.1. MNH_3 (M = In and Al)

Fig. 12(a) shows the spectrum (FWHM = 6.0 cm^{-1}) of $InNH_3$ in the range of 39400–40600 cm^{-1} [45]. Beyond this energy region, no wavelength-dependent

signals were detected. The spectrum consists of one progression with an energy interval about 230 cm^{-1}. The energy position, 39689 cm^{-1}, of the first strong band corresponds to the IE of the neutral complex. In addition, the spectrum shows a weak band (*) at 141 cm^{-1} to the red of the first strong band. A smaller feature (#) may also be identified 230 cm^{-1} above the weak band. Because their intensities depended on molecular beam source conditions, the weak bands are likely hot bands. The 230 cm^{-1} interval is well below any vibrational frequencies of ammonia and must be associated with a metal–ligand motion, which may be stretch or bend vibration. To assign these bands to the specific motion of the complex, spectral simulations were performed with the minimum energy geometries and vibrational normal modes of both association ($In–NH_3$) and insertion ($H–In–NH_2$) complexes calculated with the Gaussian 98-B3P86 DFT method [46]. The simulated spectra are shown in Fig. 12(b,c). The theoretical ionization energies are plotted relative to the position of the band origin in the experimental spectrum. It is clear from the comparison of the experimental and calculated spectra that the

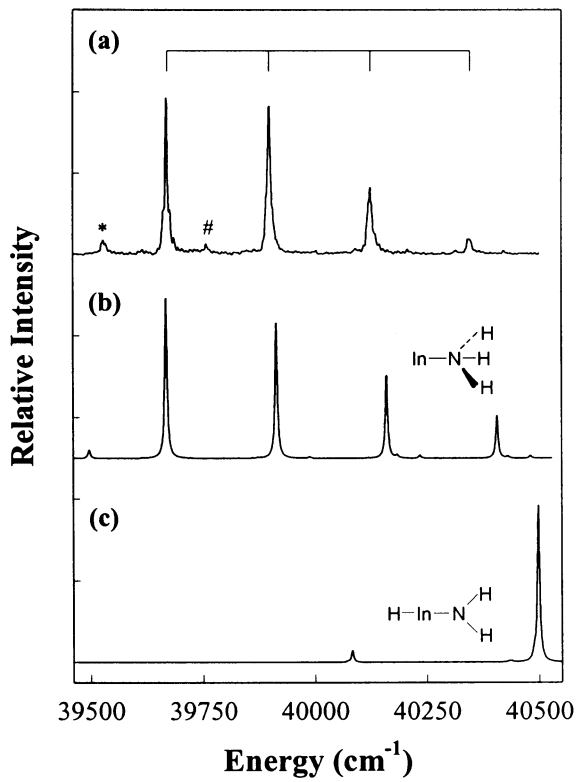

Fig. 12. Experimental (a) and simulated (b,c) ZEKE spectra of the indium–ammonia complex. The simulations were performed with the structures and vibrational frequencies calculated by the Gaussian 98-B3P86 DFT method [45].

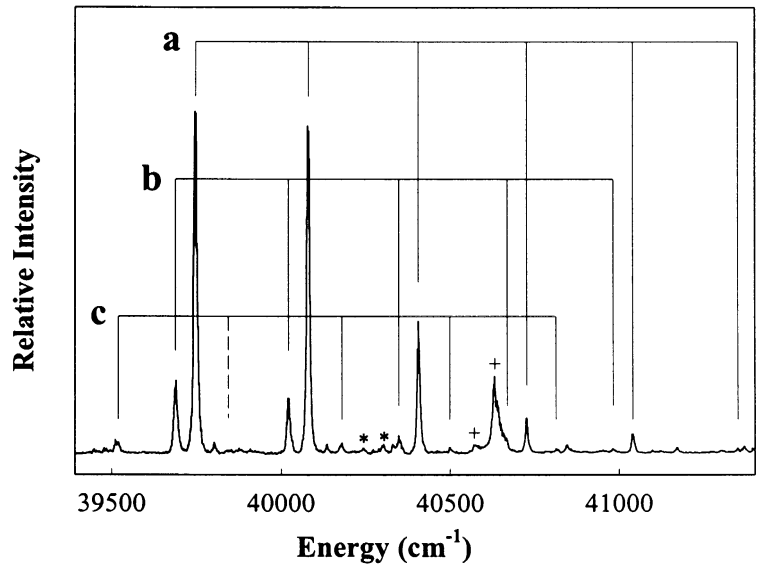

Fig. 13. ZEKE spectrum of $AlNH_3$ [47].

complex probed in the ZEKE experiment is the adduct isomer. The fact that the insertion complex $HInNH_2$ was not observed may be due to its high energy barrier and high ionization energy. The barrier was predicted to be > 30 kcal mol^{-1}, and the IE was calculated to be > 6.5 eV, which is beyond the wavelength region of our dye lasers. However, because the molecular beam is cold, the formation of a significant amount of $HInNH_2$ is unlikely. On the basis of the simulation, the 230 and 141 cm^{-1} vibrations correspond to the indium–ammonia symmetric stretches in $InNH_3^+$ and $InNH_3$. The ground state of $InNH_3^+$ is $^1A_1$ in C_{3v} symmetry, arising from the interaction between the In^+ $5s^2$ electrons and the NH_3 lone-pair. The ground state of $InNH_3$ is a Jahn–Teller distorted ^2E state, resulting from the interaction between the off-axis In p_x or p_y electron and the NH_3 lone-pair.

The ZEKE spectrum of $AlNH_3$ is more complex, as shown in Fig. 13 [47]. The spectrum mainly consists of two relatively short progressions, a and b, with the same energy interval of ca. 330 cm^{-1}. The progression b is 58 cm^{-1} to the red of the progression a. The 58 cm^{-1} spacing corresponds to the spin-orbit splitting ($^2E_{1/2}$ and $^2E_{3/2}$) of the neutral state. The spin-orbit splitting of the atomic Al in the ^2P ($3p^1$) state is 112 cm^{-1} [48]. This splitting is expected to be reduced by forming a complex because of the recoupling of the angular momentum in a molecular framework. The reduction is estimated by a factor of 1/3 in a strong field approximation (Hund's case a) [49]. Thus, the expected splitting in a Al complex is 75 cm^{-1}, which is very close to the observed values in the Al-rare gas complexes (80 cm^{-1} in AlAr and 78 cm^{-1} in AlKr) [50]. The 58 cm^{-1} splitting in $AlNH_3$ is somewhat smaller than the expected value, 75 cm^{-1}. However, spin-orbit coupling depends on atomic charges, that is, a positive charge causes a contraction of atomic

orbitals and an increase in the splitting, whereas a negative charge has an opposite effect on the splitting [49]. Thus, the smaller than the expected splitting in $AlNH_3$ indicates that Al carries a negative charge upon NH_3 coordination. This was confirmed by the Mulliken analysis, which showed a charge of -0.21 on Al. The fact that a spin-orbit splitting was not observed in the spectrum of $InNH_3$ is because the splitting of the atomic indium is so large ($^2P_{3/2} - {}^2P_{1/2} = 2212.56\ cm^{-1}$) [48] that the corresponding $^2E_{3/2}$ level in the complex was not thermally populated under the supersonic condition.

The 330 cm^{-1} interval within the progressions a and b is assigned to the aluminum–ammonia stretch in $AlNH_3^+$. In addition to the a and b progressions, there is also progression c consisting of smaller bands although the second member of the progression is very weak. This progression is associated with the metal–ligand stretch in $AlNH_3$. The stretch frequency of the neutral mode is measured to be 227 cm^{-1}. Other bands (marked with '*' and '+') may be assigned to the aluminum–ammonia bend motion in $AlNH_3^+$. This bend mode has a vibrational frequency of 557 cm^{-1}.

Table 2 summarizes the spectroscopic constants obtained from the ZEKE spectra of $AlNH_3$ and $InNH_3$. It is clear from the metal–ligand stretch frequencies that the metal ions bind ammonia much stronger than the corresponding neutral atoms. This is because the additional charge-dipole attraction and the increased dative electron donation from the nitrogen lone-pair to the aluminum atom in the ion complex. The stronger M^+–NH_3 interaction is also evident from the IE reduction of the metal atoms upon NH_3 coordination. Furthermore, aluminum binds ammonia stronger than indium, as indicated by the estimated metal–ligand stretch force constants. The force constants are converted from the metal–ligand stretch frequencies by approximating the complexes as diatomic molecules in which NH_3 is treated as a 'single atom' and by using the equation $k = 4\pi^2 c^2 \omega^2 \mu$, where ω is vibrational frequency, and μ is the reduced mass. The approximation should be reasonable because N–H vibrations within NH_3 require much higher energies than M–N stretches, and thus, the measured frequencies should be predominantly associated with the metal–ligand vibrations. The larger Al^+–NH_3 force is understandable because the higher charge density (or smaller atomic radius) of Al^+ than that of In^+ leads to stronger charge-dipole attraction between Al^+ and NH_3 than

Table 2
The IEs (cm^{-1}), metal–ligand stretch frequency (cm^{-1}), and estimated force constants (N/m) obtained from the ZEKE spectra of MNH_3 (M = In and Al) and $MO(CH_3)_2$ (M = Zr and Y)

ML	IE (M)	IE (ML)	Stretch frequency		Force constant		Reference
			M^+–L	M–L	M^+–L	M–L	
$InNH_3$	46670	39689	234	141	48	17	[45]
$AlNH_3$	48278	39746	339	227	71	32	[47]
$ZrO(CH_3)_2$	53505	42591	254	214	116	82	[52]
$YO(CH_3)_2$	50144	37997	260		121		[54]

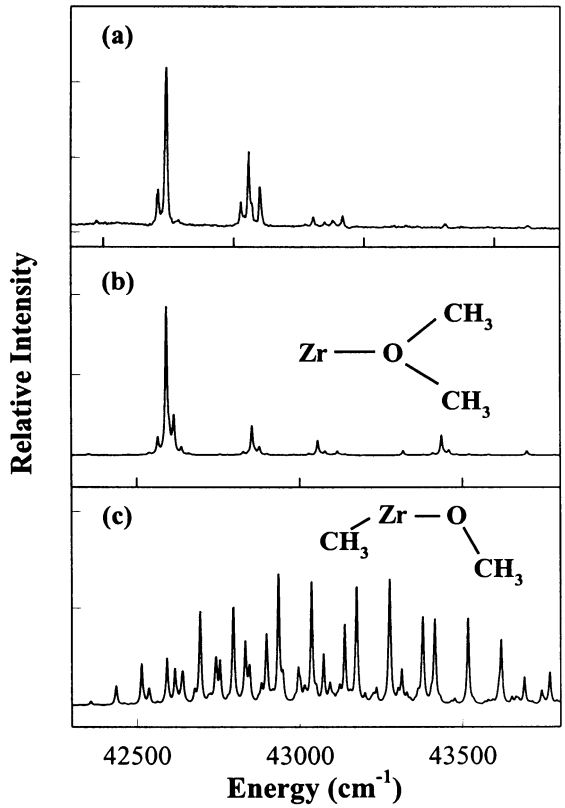

Fig. 14. Experimental (a) and simulated ZEKE spectra of the zirconium–dimethyl ether complex. The simulations were performed with the structures and vibrational frequencies calculated by the Gaussian 94-B3P86 DFT method [52].

that between In^+ and NH_3. However, the stronger Al–NH_3 interaction seems surprising from pure electrostatic viewpoint because the polarizability of the aluminum atom ($\alpha_{Al} = 6.8 \times 10^{-24}$ cm^3) is smaller than that of the indium atom ($\alpha_{In} = 10.2 \times 10^{-24}$ cm^3) [51], which would have resulted in a weaker dipole/dipole-induced interaction in Al–NH_3 than in In–NH_3. If NH_3 is assumed to bind to Al and In by partial donation of its lone pair, however, the stronger interaction in $AlNH_3$ relative to $InNH_3$ can be understood by the higher electron affinity of Al than that of In [51]. Indeed, Mulliken analysis has predicted that Al has a negative charge of -0.21, whereas In has a charge of only -0.04, and that an overlap population of 0.23 between Al and N, but no overlap between In and N.

3.3.2. $MO(CH_3)_2$ (M = Zr and Y)

Fig. 14(a) presents the ZEKE spectrum of zirconium–dimethyl ether complex [52]. Three vibrational intervals can be identified from the spectrum, which are 254, 450, and 856 cm^{-1}. By comparing with the frequencies of free dimethyl ether [53],

the 450 and 856 cm^{-1} intervals can be assigned to the COC symmetric bend and the CO symmetric stretch, respectively. The 254 cm^{-1} intervals does not match any of the symmetric modes of the ligand, it is assigned to the $Zr^{+}O$ symmetric stretch in

the ion. In addition, a 214 cm^{-1} interval can be assigned to the ZrO stretch in the neutral. The identification of the COC bend and the small metal–ligand stretch modes indicates that the complex is a weakly-bound adduct, in which the Zr atom (or Zr^{+}) binds oxygen without disrupting any of the CO bonds. The adduct structure of the complex probed in the ZEKE experiment is also supported by the spectral simulations (Fig. 14(b,c)). The simulations were calculated from the $^{4}B_{1} \leftarrow {}^{3}B_{1}$ transition of the addition structure and the $^{2}A' \leftarrow {}^{3}A''$ transition of the insertion structure, in which the Zr atom is inserted between the oxygen and carbon atoms. The comparison of the theory and experiment, although not perfect, clearly shows that the carrier of the ZEKE spectrum is the simple association complex. Although the insertion structure is ca. 80 kcal mol^{-1} lower in energy than the adduct, as predicted by Gaussian 94-B3P86, its formation has an energy barrier of 14 kcal mol^{-1}, whereas the formation of the adduct is a barrierless process. Apparently, the reaction between Zr and dimethyl ether in the supersonic jet favors the adduct structure because no energy barrier has to be overcome for its formation.

Replacing zirconium with yttrium, the ZEKE spectrum shows a stronger vibronic activity (Fig. 15) [54], implying a larger geometry change occurs upon ionization. As in the case of the zirconium complex, three vibrational modes are identified, which are $Y^{+}O$ stretch (260 cm^{-1}), COC bend (451 cm^{-1}), and CO stretch (830 cm^{-1}). In addition, the frequency of the $Y^{+}OC$ asymmetric bend is also measured to be 122 cm^{-1}. The observation of the asymmetric mode is attributed to the result of Fermi resonance interaction between the $Y^{+}OC$ asymmetric bend and the $Y^{+}O$ symmetry stretch. The Fermi interaction occurs because the first overtone frequency of the asymmetric mode is very close to the fundamental frequency of the symmetric stretch.

The IEs, stretch frequencies, and force constants are included in Table 2. Like the metal–ammonia complexes, the metal ions interact more strongly with dimethyl

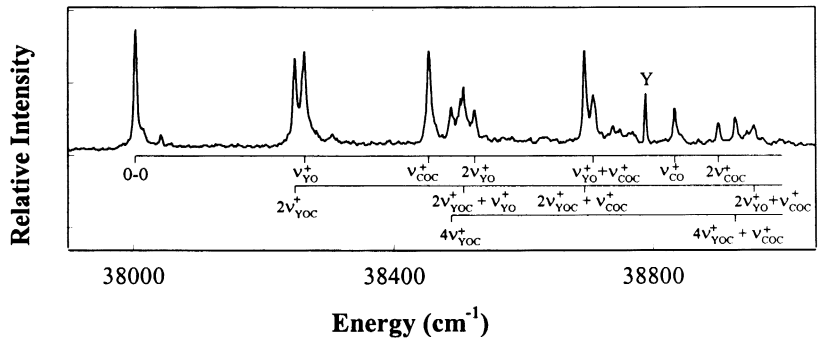

Fig. 15. ZEKE spectra of $YO(CH_3)_2$. ν^{+}_{YO}, Y^{+}–O symmetric stretch; ν^{+}_{CO}, C–O symmetric stretch; ν^{+}_{COC}, C–O–C symmetric bend; and ν^{+}_{YOC}, Y^{+}–O–C asymmetric bend in $[YO(CH_3)_2]^{+}$ [54].

ether than the corresponding neutral atoms, as indicated by the lower IEs of the complexes than that of the metal atoms and by the higher metal–ether stretch frequencies in the ion complexes. It is noted, however, that the M^+–$O(CH_3)_2$ bonding is similar in the zirconium and yttrium complexes, as shown by the force constants of metal ion-ligand stretch vibrations.

4. Concluding remarks

I have tried to show that ZEKE PES can offer new opportunities in studying inorganic and organometallic molecules. The ZEKE technique has the resolution to resolve close-lying vibrational levels and even rotational levels in some cases. Geometries and electronic states of the neutral and ionic species can be determined by combining the vibrationally resolved spectra with quantum chemical calculations and spectral simulations.

A major requirement in ZEKE experiments is the use of tunable light source. So far, frequency-doubled dye lasers have been used mostly in studying metal compounds. It is possible to use vacuum ultraviolet laser and synchrotron radiation to metal compounds, as they have already been employed in studying nonmetal-containing molecules [55,56].

Acknowledgements

The author wish to thank his current coworkers at the University of Kentucky and former colleagues at the National Research Council of Canada (NRC Canada) whose names appear on the papers quoted herein. He is especially indebted to Dr P.A. Hackett, who gave great support to the metal cluster project at NRC Canada. Partial support for the work on metal–molecule complexes is provided by the Donors of The Petroleum Research Fund, administrated by the American Chemical Society.

References

[1] D.W. Turner, C. Baker, A.D. Baker, C.R. Brundle, Molecular Photoelectron Spectroscopy, Wiley, New York, 1970.
[2] A.H. Cowley, Prog. Inorg. Chem. 26 (1979) 46.
[3] J.C. Green, Struct. Bond. (Berlin) 43 (1981) 37.
[4] A. Oskam, in: J.H. Clark, R.E. Hester (Eds.), Spectroscopy of Inorganic Based Materials, Wiley, New York, 1987, p. 429.
[5] D.L. Lichtenberger, G.E. Kellogg, Acc. Chem. Res. 20 (1987) 379.
[6] G.M. Bancroft, Y.F. Hu, in: E.I. Solomon, A.B.P. Lever (Eds.), Inorganic Electronic Structure and Spectroscopy, vol. 1, Wiley, New York, 1999, p. 443.
[7] K. Müller-Dethlefs, E.W. Schlag, Ann. Rev. Phys. Chem. 42 (1991) 109.
[8] K. Müller-Dethlefs, E.W. Schlag, E.R. Grant, K. Wang, B.V. McKoy, in: S.A. Rice, I. Prigogine (Eds.), Advances in Chemical Physics, vol. XC, Wiley, New York, 1995, p. 1.

[9] K. Müller-Dethlefs, E.W. Schlag, Angew. Chem. Int. Ed. 37 (1998) 1346.
[10] E.W. Schlag, ZEKE Spectroscopy, Cambridge University Press, Cambridge, 1998.
[11] G.F. Gantefor, D.M. Cox, A. Kaldor, J. Chem. Phys. 93 (1990) 8395.
[12] G.F. Gantefor, D.M. Cox, A. Kaldor, J. Chem. Phys. 96 (1992) 4102.
[13] G. Drechsler, C. Bäβmann, U. Boesl, E.W. Schlag, J. Mol. Struct. 348 (1995) 337.
[14] G. Drechsler, U. Boesl, C. Bäβmann, E.W. Schlag, J. Chem. Phys. 107 (1997) 2284.
[15] D.S. Yang, M.Z. Zgierski, D.M. Rayner, P.A. Hackett, A. Martinez, D.R. Salahub, P.N. Roy, T. Carrington, Jr., J. Chem. Phys. 103 (1995) 5335.
[16] D.S. Yang, P.A. Hackett, J. Electron Spectrosc. Relat. Phenom. 106 (2000) 153.
[17] D.S. Yang, A.M. James, D.M. Rayner, P.A. Hackett, J. Chem. Phys. 102 (1995) 3129.
[18] T.G. Dietz, D.E. Powers, M.A. Duncan, R.E. Smalley, J. Chem. Phys. 74 (1981) 6511.
[19] D. Proch, T. Trickl, Rev. Sci. Instrum. 60 (1989) 713.
[20] W.C. Wiley, I.H. McLaren, Rev. Sci. Instrum. 26 (1955) 1150.
[21] P.R.R. Langridge-Smith, M.D. Morse, G.P. Hansen, R.E. Smalley, A.J. Merer, J. Chem. Phys. 80 (1984) 593.
[22] A.J. James, P. Kowalczyk, E. Langlois, M.D. Campbell, A. Ogawa, B. Simard, J. Chem. Phys. 101 (1994) 4485.
[23] B. Simard, A.M. James, P. Kowalczyk, R. Fournier, P.A. Hackett, Proc. SPIE 376 (1994) 2124.
[24] G. Herzberg, Molecular Spectra and Molecular Structure, vol. 1, 2nd ed., Krieger, Malabar, 1989, p. 214.
[25] J. Xie, R.N Zare, J. Chem. Phys. 93 (1990) 3033.
[26] J.L Femenias, G. Cheval, A.J. Merer, U. Sassenberg, J. Mol. Spectrosc. 124 (1987) 348.
[27] J.M. Dyke, A.M. Ellis, M. Feher, A. Morris, A.J. Paul, J.C.H. Stevens, J. Chem. Soc. Faraday Trans. Sect. II 83 (1987) 1555.
[28] DEMON-KS was developed at the University of Montreal. M.E. Casida, C. Daul, A. Goursot, A. Koester, L. Pettersson, E. Proynov, A. St-Amant, D.R. Salahub, H. Duarte, N. Godbout, J. Guan, C. Jamorski, M. Leboeuf, V. Malkin, O. Malkina, F. Sim, A. Vela.
[29] T.E. Sharp, H.M. Rosenstock, J. Chem. Phys. 41 (1964) 3452.
[30] F. Duschinsky, Acta Physicochim. URSS 7 (1937) 551.
[31] (a) E.V. Doktorov, I.A. Malkin, V.I. Man'ko, J. Mol. Spectrosc. 64 (1977) 302. (b) E.V. Doktorov, I.A. Malkin, V.I. Man'ko, J. Mol. Spectrosc. 56 (1975) 1.
[32] M.Z. Zgierski, Chem. Phys. 108 (1986) 61.
[33] M.Z. Zgierski, F. Zerbetto, J. Chem. Phys. 99 (1993) 3721.
[34] D.S. Yang, M.Z. Zgierski, A. Bérces, P.A. Hackett, P.N. Roy, A. Martinez, T. Carrington, Jr., D.R. Salahub, R. Fournier, T. Pang, C. Chen, J. Chem. Phys. 105 (1996) 10663.
[35] Gaussian 94/DFT (Revision G.4), M.J. Frisch, G.W. Trucks, H.B. Schlegel, P.M.W. Gill, B.G. Johnson, M.W. Wong, J.B. Foresman, M.A. Robb, M. Head-Gordon, E.S. Replogle, R. Gomperts, J.L. Andres, K. Raghavachari, J.S. Binkley, J.J.P. Stewart, J.A. Pople, Gaussian, Inc., Pittsburgh PA, 1993.
[36] D.S. Yang, M.Z. Zgierski, P.A. Hackett, J. Chem. Phys. 108 (1998) 3591.
[37] D.S. Yang, M.Z. Zgierski, A. Bérces, P.A. Hackett, A. Martinez, D.R. Salahub, Chem. Phys. Lett. 277 (1997) 71.
[38] M. Knickelbein, S. Yang, J. Chem. Phys. 93 (1990) 5760.
[39] M. Knickelbein, J. Chem. Phys. 102 (1995) 1.
[40] D.S. Yang, (unpublished results).
[41] C.A. Arrington, T. Blume, M.D. Morse, M. Doverstal, U. Sassenberg, J. Phys. Chem. 98 (1994) 1398.
[42] G. Verhaegen, S. Smoes, J. Drowart, J. Chem. Phys. 40 (1964) 239.
[43] H. Wang, T. Craig, H. Haouari, Y. Liu, J.R. Lombardi, D.M. Lindsay, J. Chem. Phys. 105 (1996) 5355.
[44] H. Haouari, H. Wang, R. Craig, J.R. Lombardi, D.M. Lindsay, J. Chem. Phys. 103 (1995) 9527.
[45] G.K. Rothschopf, J.S. Perkins, S. Li, D.S. Yang, J. Phys. Chem. 104 (2000) 8178.
[46] Gaussian 98 (Revision A.2), M.J. Frisch, G.W. Trucks, H.B. Schlegel, G.E. Scuseria, M.A. Robb, J.R. Cheeseman, V.G. Zakrzewski, J.A. Montgomery, R.E. Stratmann, J.C. Burant, S. Dapprich,

J.M. Millam, A.D. Daniels, K.N. Kudin, M.C. Strain, O. Farkas, J. Tomasi, V. Barone, M. Cossi, R. Cammi, B. Mennucci, C. Pomelli, C. Adamo, S. Clifford, J. Ochterski, G.A. Petersson, P.Y. Ayala, Q. Cui, K. Morokuma, D.K. Malick, A.D. Rabuck, K. Raghavachari, J.B. Foresman, J. Cioslowski, J.V. Ortiz, B.B. Stefanov, G. Liu, A. Liashenko, P. Piskorz, I. Komaromi, R. Gomperts, R.L. Martin, D.J. Fox, T. Keith, M.A. Al-Laham, C.Y. Peng, A. Nanayakkara, C. Gonzalez, M. Challacombe, P.M.W. Gill, B.G. Johnson, W. Chen, M.W. Wong, J.L. Andres, M. Head-Gordon, E.S. Replogle, J.A. Pople, Gaussian, Inc., Pittsburgh PA, 1998.

[47] D.S. Yang, J. Miyawaki, Chem. Phys. Lett. 313 (1999) 514.

[48] C.E. Moore, Atomic Energy Levels, Natl. Stand. Ref. Data Ser. No. 35, Natl. Bur. Stand., Washington, DC, 1971.

[49] H. Lefebvre-Brion, R.W. Field, Perturbations in the Spectra of Diatomic Molecules, Academic Press, Orlando, FL, 1986.

[50] C.L. Challender, S.A. Mitchell, P.A. Hackett, J. Chem. Phys. 90 (1989) 5252.

[51] D.R. Lide, H.P.R. Frederikse (Eds.), CRC Handbook of Chemistry and Physics, 78th ed., CRC Press, New York, 1997.

[52] D.S. Yang, M.Z. Zgierski, P.A. Hackett, unpublished result.

[53] L.M. Sverdlov, M.A. Kovner, E.P. Krainov, Vibrational Spectra of Polyatomic Molecules, Wiley, New York, 1974, p. 477.

[54] D.S. Yang, unpublished result.

[55] W. Kong, J.W. Hepburn, J. Phys. Chem. 99 (1995) 1637.

[56] C.-W. Hsu, P. Heimann, M. Evans, S. Stimson, P.T. Fenn, C.Y. Ng, J. Chem. Phys. 106 (1997) 8931.